eprints@whiterose.ac.uk
https://eprints.whiterose.ac.uk/

Synthesis and characterisation of the new oxyfluoride Li$^+$ ion conductor, Li$_5$SiO$_4$F

Bo Dong[†,*], Jinhui Yan[†], Brant Walkley[†], Kenneth K. Inglis[‡], Frédéric Blanc[‡,§,*], Stephen Hull[⊥], Anthony R. West[†,*]

† University of Sheffield, Department of Material Science and Engineering, Mappin Street, Sheffield S1 3JD, UK

‡ University of Liverpool, Department of Chemistry, Crown Street, Liverpool L69 7ZD, UK

§ University of Liverpool, Stephenson Institute for Renewable Energy, Crown Street, Liverpool, L68, 7ZD, UK

⊥ The ISIS Facility, STFC, Rutherford-Appleton Laboratory, Didcot, Oxfordshire OX11 0QX, UK

ABSTRACT: A new polymorphic phase, Li$_5$SiO$_4$F, with Li$^+$ ion dynamics that are structurally distinct from Li$_4$SiO$_4$, is described. The γ polymorph forms at 750-775 °C, melts incongruently at 800 °C and crystallizes in a monoclinic unit cell: a = 8.67(1) (Å), b = 16.51(1) (Å), c = 11.23(2) (Å), β = 96.61(4) (°) and V = 1602.3(3) (Å^3). The α polymorph forms at 650 °C and appears to be metastable. The γ polymorph has a Li$^+$ ion conductivity of 1.2x10^{-7} Scm^{-1} at 40 °C, that is several orders of magnitude higher than both the α polymorph and Li$_4$SiO$_4$, with an associated activation energy of 0.51(1) eV. Variable temperature ^{19}F and ^{7}Li static NMR measurements show the absence of F$^-$ mobility but the existence of Li$^+$ mobility and confirm that Li$^+$ is the main charge carrier in both polymorphs of Li$_5$SiO$_4$F. ^{7}Li line narrowing NMR experiments suggest that the barrier to local Li hopping is fairly small (0.2-0.3 eV) with faster Li$^+$ ion dynamics in γ-Li$_5$SiO$_4$F compared to α-Li$_5$SiO$_4$F. γ-Li$_5$SiO$_4$F has negligible electronic conductivity, is stable in contact with Li metal and is a new type of stoichiometric, mixed anion, Li$^+$ ion conductor.

INTRODUCTION

Batteries are increasingly used in electrical storage systems to store energy from intermittent sources (e.g. solar and wind) within electrical power grids and for electric or hybrid electric vehicle propulsion.[1] Safety issues associated with lithium batteries are usually caused by the organic liquid electrolyte, which may become flammable when lithium dendrite formation occurs during battery cycling, leading to short circuiting and overheating.[2] One solution to this issue involves the use of solid electrolytes; however, additional problems may then arise due to (i) the low conductivity of most potential lithium solid electrolytes and (ii) high impedance associated with solid-solid interfaces in an all-solid-state lithium battery.

For many years, there has been significant interest in doped Li$_4$SiO$_4$ and related LISICON (derived from LIthium SuperIonic CONductor) materials as solid electrolytes,[3-6] with the commercialisation of a thin film, solid state lithium battery using LIPON (lithium phosphorus oxynitride) solid electrolyte.[7] Li$_4$SiO$_4$ is stable in contact with a lithium metal anode but its conductivity is too low (less than 10^{-10} Scm^{-1} at 25 °C)[8] for practical applications.[9] Many doping studies of Li$_4$SiO$_4$ and related materials have been carried out,[9] leading to enhanced conductivity. These have usually involved cation doping within a fixed oxide framework; the enhanced conductivity is associated with either Li interstitials or Li vacancies which arise due to charge compensation of aliovalent dopants.[10] Considering the similar sizes of the O^{2-} and F$^-$ ions (octahedral radii of 1.26 Å for O^{2-} and 1.19 Å for F$^-$)[11], several oxyfluoride cathode (LiFeSO$_4$F[12] and LiFePO$_4$F[13]) and anode

materials (Li_2VO_2F[14] and KNb_2O_5F[15]) have been successfully synthesised and showed enhanced capacities and cyclabilities. In contrast, the possibility of aliovalent anion doping of solid state electrolyte materials, such as Li_4SiO_4, has been little studied.

During an unsuccessful attempt to dope Li_4SiO_4 with LiF, we have instead, prepared a new phase, Li_5SiO_4F, whose high temperature γ polymorph has comparable Li^+ ion conductivity to cation-doped Li_4SiO_4 materials. This is the first example of a high lithium ion conductivity solid electrolyte in a silicate-fluoride system and demonstrates the potential of such mixed anion systems for novel solid electrolyte applications. In this paper, we report the synthesis of Li_5SiO_4F, the existence of two polymorphs (α and γ) and the Li^+ ion dynamics of both phases using impedance spectroscopy and variable temperature ^7Li NMR experiments. The results obtained from impedance spectroscopy give bulk conductivity data but cannot always explicitly identify the conducting species. The temperature dependent ^7Li NMR line width and spin-lattice relaxation rates, which are very sensitive to Li^+ mobility, show explicitly that Li^+ is the charge carrier in both phases of Li_5SiO_4F and highlight the faster Li^+ ion mobility of the γ phase over the α phase in this new Li^+ ion solid electrolyte.

EXPERIMENTAL

Li_2CO_3 (Sigma-Aldrich, 99%), SiO_2 (Alfa Aesar, 99.5%) and LiF (Alfa Aesar, 99%) starting materials were dried at 180 °C and stored in a desiccator. As an exploration into the possible doping of Li_4SiO_4 with LiF and subsequently into compound formation, numerous samples in the composition triangle Li_2O-LiF-SiO_2 were prepared (Table Supplementary 1). The starting materials were weighed according to the desired stoichiometry, ground with a mortar and pestle using acetone for 30 min, dried, pressed at 15 MPa for 1 min into pellets of diameter 9.8 mm and thickness 1-2 mm, placed in a gold boat and transferred to a muffle furnace. Pellets were heated at 400 °C (heating rate, 5 °C/min) for 2 h to drive off CO_2, cooled to room temperature, reground, repelleted and heated to temperatures in the range 600 to 800 °C (heating rate, 5 °C/min) for 10 h. The α- and γ- forms of Li_5SiO_4F were obtained at 650 and 750-775 °C, respectively, with each temperature chosen to yield products that did not change on prolonged heating.

A Bruker D2 X-ray diffractometer with Cu Kα radiation (λ= 1.5418 Å) was used for phase identification. Patterns were recorded over the range 15° to 80°. For indexing, a Stoe STADI P X-ray diffractometer with Cu Kα1 radiation (λ=1.5406 Å) and a linear position sensitive detector (PSD) was used with WinXpow and PDF 2016 software.

Pellets for impedance measurements were sintered at their synthesis temperature for 4 h before coating opposite faces with Au paste to form electrodes and attached to the Pt leads of a conductivity jig which was placed inside a horizontal tube furnace. Impedance data were recorded in air with a Solartron analyser, model 1260 with 100 mV *ac* voltage and frequency range 10^{-2} to 10^6 Hz.

DSC data were collected using a NETZSCH 404C instrument at 10 °C/min heating/cooling rate under 50/50 Ar/air atmosphere. Data were analysed using Proteus Analysis software. X-ray fluorescence (XRF) measurements were carried out with a PANalytical Zetium Spectrometer using a Rh X-ray tube.

For electrochemical testing, the new phase Li_5SiO_4F, was pressed into 1 mm thick pellets and heated at 750 °C for 4 h. A half-cell, Li/Li_5SiO_4F/Li, was constructed using a Swagelok test cell. Cyclic voltammetry was carried out between 0 V and 6 V in 10 mV steps for two cycles using a Perkin-Elmer VMP tester.

Solid-state NMR experiments were obtained at 9.4 T on a Bruker Avance III HD spectrometer. Variable temperature ^7Li static spectra were collected with a Bruker 4 mm HXY Magic Angle Spinning (MAS) probe in double resonance mode below 21 °C and with a Bruker 4 mm HX high temperature MAS probe between 21 and 380 °C with the X channel tuned to ν_0(^7Li) = 155.5 MHz. ^7Li spectra were obtained with a π/2 pulse of 1.5

μs at a rf amplitude of $\nu_1(^7Li)$ = 83 kHz. Spin-lattice relaxation rates (T_1^{-1}) were obtained with a saturation recovery pulse sequence and fitted to a reverse exponential of the form: $1 - \exp(-\tau/T_1)^a$, where τ and a are variable delays and the stretched exponential coefficient (between 0.75 and 1), respectively. Spin-lattice relaxation rates in the rotating frame ($T_{1\rho}^{-1}$) were obtained with a spin-lock experiment of form: $\pi/2 - \tau_{spin-lock} -$ acq, at spin-lock frequencies of $\nu_1(^7Li)$ = 20, 33 and 50 kHz and data fitted to a stretched exponential of the form: $\exp(-\tau/T_{1\rho})^a$, where a was set between 0.5 and 1.

Variable temperature ^{19}F NMR static spectra were obtained with a Bruker 4 mm HX high temperature MAS probe between 21 and 150 °C with the ^1H channel detuned to $\nu_0(^{19}F)$ = 376.5 MHz. ^{19}F static spectra were obtained with $\pi/2$ pulses at an rf amplitude of $\nu_1(^{19}F)$ = 83 kHz. ^{19}F fast MAS spectra were recorded with a Bruker 1.3 mm HXY MAS probe (in double resonance mode) with the ^1H channel detuned to $\nu_0(^{19}F)$ = 376.5 MHz and using a pulse – acquire sequence with $\pi/2$ pulses at an rf amplitude of $\nu_1(^{19}F)$ = 200 kHz. Quantification of the fluoride content from fast MAS data used the CF_3CH_2OH reference as an external standard. Temperature calibrations were performed with the ^{207}Pb chemical shift thermometer $Pb(NO_3)_2$ [16-17] and by following the γ-to-β phase transition of CuI at 369 °C using ^{63}Cu NMR.[18-19] All temperatures reported are actual sample temperatures with an estimated accuracy of ± 5 °C between -163 and 147 °C and ± 10 °C between 147 and 377 °C. All spectra were obtained under quantitative conditions (with recycle delays longer than 5x the spin lattice relaxation times T_1). ^7Li and ^{19}F spectra were referenced to 10 M LiCl in D_2O at 0 ppm and neat CF_3CH_2OH at -77.03 ppm (corresponding to $CFCl_3$ at 0 ppm).[20]

RESULTS AND DISCUSSION

Synthesis and characterization of Li_5SiO_4F

Initial attention focused on the possible synthesis of F-doped Li_4SiO_4 but it became apparent that, instead of successful doping, other previously-unreported phases were showing up in the XRD results, with indications of enhanced lithium ion conductivity from preliminary conductivity measurements. An exploratory study of compound formation in the system Li_2O-SiO_2-LiF was required to isolate the highly conducting new phase.

The results of solid state reaction between Li_2O (using Li_2CO_3 as starting material), LiF and SiO_2 fell into two groups, depending on the overall composition, as shown in the ternary composition triangle, Fig. 1. Compositions bounded by Li_2O, Li_2SiO_3 and LiF could be heated safely to 800 °C without loss of fluoride, as evidenced by XRF data (Table 1) and ^{19}F MAS spectra (Fig. S1). XRD analysis of the products of heating a range of compositions in this area, Table S1 and Fig. S2, showed the formation of a new phase which was phase-pure at the composition Li_5SiO_4F. Results of the XRF analysis of γ-Li_5SiO_4F, Table 1, match the expected sample composition, within error. Additionally, the ^{19}F MAS spectra recorded against an external standard show the presence of one fluoride (± 0.1) per formula unit. Both datasets confirmed the Li_5SiO_4F composition and therefore, that compositions in this region of the ternary composition triangle can be reacted satisfactorily without loss of fluoride or lithium.

Li_5SiO_4F is polymorphic, Fig. 2; the form labelled α is the reaction product at ~ 650 °C and the form labelled γ is the reaction product at ~ 750 °C. Transformation of the α to γ polymorph occurs at temperatures above ~ 650 °C and is not reversible on reheating the γ polymorph at 600-650 °C, indicating that the α polymorph is probably metastable. The α to γ transformation was not accompanied by any significant weight loss, as shown by weight measurements on a sample before and after transformation and therefore, the α form is not an oxy-carbonate phase. The γ form melts at ~793 °C, as shown by DSC, Fig. 3, with a sharp endotherm on heating at ~793 °C. XRD patterns recorded after brief melting at 850 °C followed by rapid cooling showed a mixture of phases including Li_4SiO_4 and LiF. This indicates that melting of Li_5SiO_4F is incongruent; if the melting were

congruent then instead, γ-Li$_5$SiO$_4$F should be the main product of crystallization on cooling. The exotherm observed on cooling at~758 ^{o}C, Fig. 2, is attributed to crystallization of the liquid in the fully or partially melted sample.

XRD data for γ-Li$_5$SiO$_4$F were indexed on a monoclinic unit cell with a = 8.67(1) (Å), b = 16.51(1) (Å), c = 11.23(2) (Å), β = 96.61(4) (^{o}) and V = 1602.3(3) (Å^3), Table S2. All lines shown for γ-Li$_5$SiO$_4$F in Fig. 2 were indexed and were well within a Δ2θ difference window of 0.05^o for experimental and calculated peak positions. We do not know the structure of γ-Li$_5$SiO$_4$F and the pattern of α is, as-yet, unindexed.

The structures of γ and α polymorphs are not solid solutions derived from Li$_4$SiO$_4$, as their XRD data are significantly different from that of Li$_4$SiO$_4$ (Fig. 2) and are different from that of any other known lithium silicate phase. There is no unreacted LiF present (Fig. 2) as also confirmed by the ^{19}F MAS NMR spectra of both polymorphs (Fig. S1) which does not show the known ^{19}F signal of LiF (expected at -204 ppm).[21] From the formula Li$_5$SiO$_4$F, we anticipate that the structure contains two anions, SiO$_4^{4-}$ and F$^-$, without any replacement of O by F in the silicate tetrahedra.

Electrical properties

Impedance data for γ-Li$_5$SiO$_4$F with gold electrodes at different temperatures in air are shown in Fig. 4. The impedance complex plane plots (a-d) consist of a high frequency arc and a low frequency inclined spike, which starts to show curvature at the highest temperatures (d). M''/Z'' spectroscopic plots for one temperature, 95 °C, (e) show overlapping high frequency peaks. Since M'' peaks represent the component of the sample with the smallest capacitance, which is usually the bulk component, this indicates that the Z'' peak, and the associated Z* arc, also represent the bulk response of the sample.

C' spectroscopic plots (f) show a limiting high frequency capacitance, C with value 4 x 10^{-12} Fcm^{-1}. This corresponds to the bulk permittivity ε$_\infty$', with a value, 45.2, given by ε$_\infty$' = C/ε$_0$, where ε$_0$ is the permittivity of free space, 8.854 x 10^{-14} Fcm^{-1}. The C' data also show a partially-resolved intermediate frequency plateau, of value ~8 x 10^{-12} Fcm^{-1} and a large increase at lower frequencies to values approaching 10^{-5} Fcm^{-1}. The intermediate frequency plateau is unlikely to represent a grain boundary contribution to the impedance since its value is much smaller than expected for a typical grain boundary whose capacitance, based on geometric considerations, is usually 1-3 orders of magnitude larger than the bulk capacitance.

An alternative possibility is that the intermediate frequency plateau represents a dipole contribution to the *ac* conductivity, similar to that which has been evidenced recently in impedance data of yttria-stabilized zirconia, YSZ.[22-23] Dipolar processes do not contribute to long range *dc* conduction; they are represented, ideally, by an equivalent circuit that contains a resistance, R in series with a blocking capacitance, C. Conduction processes, by contrast, are represented by a parallel combination of a resistance, capacitance and constant phase element, CPE; the CPE is required to model deviation from ideal, Debye-like behaviour and effectively, is a parallel combination of a frequency-dependent resistor and frequency-dependent capacitor.

The new circuit element used to model the high frequency part of the bulk impedance data of YSZ[23] is a combination, in parallel, of the element that represents bulk *dc* conduction, R$_1$, C$_1$, CPE$_1$ and an element that represents dipolar processes, R$_2$, C$_2$. This forms the left side part of the master equivalent circuit shown in Fig. 5. Inclusion of the dipole element R$_2$, C$_2$, in Fig. 5 does not affect the magnitude of the *dc* conductivity, R$_1^{-1}$, whose value is obtained from the intercept of the arc or low frequency spike on the Z' axis of the Z* plots, Fig. 4 (a).

In order to model the low frequency, inclined spike in the impedance complex plane plots (a-d) and the large increase in capacitance seen at low frequencies (f), an additional element in the equivalent circuit is required

that is in series with the bulk element. This additional element represents blocking of ionic conduction, in this case of Li^+ ions (confirmed by NMR measurements, discussed below) across the sample-electrode interface, but is not a simple capacitor since the angle to the real, Z' axis of the inclined spike is less than 90º. Instead, a second constant phase element, CPE_3 is required in the equivalent circuit, Fig. 5. At higher temperatures, the low frequency impedance data show curvature in the inclined spike which indicates that CPE_3 is terminated at the lowest frequencies by a finite parallel resistance, R_3.

Impedance data were fitted to the equivalent circuit, Fig. 5, using ZView software,[24] but for any given data set, the frequency range was insufficient to allow all parameters in the master circuit (Fig. 5) to be varied. At lower temperatures, component R_3 was too large to be detected and refined and was excluded from the fit shown in Fig. 6. By contrast, at higher temperatures, element C_1 (fixed at 1 pF cm^{-1}) was excluded from refinement of the fit shown in Fig. 7.

Fig. 8 shows Arrhenius plots of the bulk conductivities, R_1^{-1}, of α-, γ-Li_5SiO_4F and, for comparison, Li_4SiO_4. Conductivities and activation energies of α-Li_5SiO_4F and Li_4SiO_4 are similar whereas the conductivity of γ-Li_5SiO_4F is several orders of magnitude higher, especially at lower temperatures and with a smaller activation energy, 0.51(1) eV. γ-Li_5SiO_4F is therefore, an entirely new Li^+ ion conductor, that is structurally distinct from Li_4SiO_4 and its doped derivatives. γ-Li_5SiO_4F is a stoichiometric phase and not a solid solution derived from Li_4SiO_4 whose conductivity has been increased by doping. It may, therefore, be amenable to conductivity enhancement by suitable doping.

Inclusion of R_3 in analysis of the higher temperature data gives a method to estimate ionic, t_i and electronic, t_e transport numbers because the existence of R_3 implies a finite, *dc* leakage current through the sample-electrolyte combination. Since discharge of Li^+ ions is regarded as unlikely at these temperatures, R_3 provides an estimate of the residual electronic conductivity of the sample. Since $R_3 >> R_1$, we make the assumption that R_1 is the ionic resistance, R_3 is the electronic resistance and calculate the electronic transport number from the ratio $R_1:R_3$. This gives a value, for the data shown in Fig. 7, of t_e = 0.005 at 143 ºC.

Cyclic voltammetry tests were carried out at room temperature on pellets of γ-Li_5SiO_4F over the voltage range 0 – 6V, with the following observations: the colour of γ-Li_5SiO_4F remained white over several cycles; there was no indication of any significant redox processes occurring for biases up to 6 V, Fig. 9; the XRD pattern of γ-Li_5SiO_4F did not change after the CV test. These observations are a good indication that γ-Li_5SiO_4F is stable in contact with Li metal, unlike titanate-based perovskites such as $Li_{(0.5+3x)}La_{(0.5-x)}TiO_3$ which reduce readily in contact with Li metal. The sensitivity of the equipment used to record the I-V plot in Fig. 9, showed a small current was detected with increasing voltage, from which the resistance of the sample-electrode combination under those conditions was estimated. The value obtained, ~ 15 MΩ at room temperature, is comparable to that estimated by extrapolation of the Arrhenius plot to 25 ºC of 38 MΩ. It therefore corresponds approximately to the bulk resistance R_1. The relatively short timescales used to record data points for the I/V plot were insufficient to be able to detect R_3 in the I/V data.

NMR spectroscopy

Information regarding Li^+ ion dynamics of both α- and γ-Li_5SiO_4F phases were obtained from variable temperature ^7Li static NMR spectra, Fig. 10. At room temperature, both phases show a complex NMR line shape typical of ^7Li in various overlapping environments containing the ^7Li–^7Li dipolar broadened central transition (+1/2 ↔ −1/2) with full width at half-maximum (fwhm) of ~13.5 and ~13 kHz for α-Li_5SiO_4F and γ-Li_5SiO_4F, respectively, along with the ^7Li satellite transitions observed at ~ ± 500 ppm. Below room temperature, the ^7Li central NMR line of γ-Li_5SiO_4F broadens (fwhm ~13.6 kHz), highlighting the presence of Li mobility under ambient conditions. As temperature increased, the central transition narrows further,

indicating averaging of the ^{7}Li–^{7}Li dipolar interactions due to an increase in Li$^+$ mobility, Fig. 11 (a). The onset of this motional narrowing of the NMR line widths is observed at 24 ^{o}C for γ-Li$_5$SiO$_4$F, at much lower temperature than that of α-Li$_5$SiO$_4$F (126 ^{o}C), highlighting the faster Li$^+$ diffusion in γ-Li$_5$SiO$_4$F.

At the inflection point of the temperature-dependent line narrowing, Fig. 11 (a), the Li$^+$ jump rate τ^{-1} is estimated from the NMR line width at fwhm in the low temperature rigid-lattice regime, $\Delta_{\omega \text{rigid lattice}}$. The inflection points are obtained using a sigmoidal regression fit and jump rates τ^{-1} of ~8.5(1) × 10^4 and ~8.6(1) × 10^4 s^{-1} at 220 and 130 ^{o}C for α-Li$_5$SiO$_4$ and γ-Li$_5$SiO$_4$F are extracted, respectively. The onset of motional narrowing occurs at a much lower temperature for γ-Li$_5$SiO$_4$F than α-Li$_5$SiO$_4$F, and indicates faster Li$^+$ ion dynamics in the former phase. When compared to Li$_4$SiO$_4$, the onset of Li$^+$ motion occurs at ~100 ^{o}C, highlighting the faster Li$^+$ ion dynamics in γ-Li$_5$SiO$_4$F.[25] Note that within a similar temperature window, the ^{19}F static NMR lineshape of both phases remain constant (fwhm ~35 kHz) suggesting the absence of mobile fluoride ions, Fig. 12.

The temperature dependence of ^{7}Li spin-lattice relaxation (SLR) rates in the laboratory frame (T_1^{-1}) and the rotating frame ($T_{1\rho}^{-1}$) for α-Li$_5$SiO$_4$F and γ-Li$_5$SiO$_4$F are shown in Fig. 11 (b). The changes in relaxation rates arise from changes in the local magnetic interactions through increased Li ion mobility and hence provide information on Li$^+$ ion dynamics on the orders of the Larmor (MHz) and spin-lock frequencies (kHz) for SLR experiments.[26-27]

In α-Li$_5$SiO$_4$F, $T_{1(\rho)}^{-1}$ values are relatively temperature-independent below room temperature, highlighting little Li mobility. Above 120 ^{o}C, $T_{1(\rho)}^{-1}$ rates increase as the temperature increases, and indicate the ^{7}Li slow motional regime ($\omega\tau c \gg 1$ where ω and τ_c are the probed frequencies and correlation times of the motion, respectively). Using the Arrhenius equation, activation barriers of 0.20(1) and 0.30(2) eV are extracted from the low-temperature flanks of the T_1^{-1} and $T_{1\rho}^{-1}$ rates, respectively. Here, in this regime, the $T_{1(\rho)}^{-1}$ values are characteristic of local processes such as hops between local energy minima that may contribute to unsuccessful jumps to neighbouring Li sites.[26, 28-29] These energy barriers do not probe long range translational Li$^+$ diffusion and are therefore not directly comparable with the results obtained with the conductivity data given above (Fig. 5).

In the case of γ-Li$_5$SiO$_4$F, $T_{1(\rho)}^{-1}$ values below -60 ^{o}C vary weakly with temperature. Between -60 and 60 ^{o}C, $T_{1\rho}^{-1}$ rates increase and a small activation barrier of 0.08(1) eV was obtained. This value is very small and probably probes atomic vibration rather than Li diffusion, which is not observed in T_1^{-1} values due to the shorter timescale probed. Above 60 ^{o}C, both T_1^{-1} and $T_{1\rho}^{-1}$ rates increase with temperature, indicating a slow motional regime and local Li$^+$ hops with activation barriers of 0.22(1) and 0.21(1) eV, respectively.

Fig. 11 (b) also gives the SLR data obtained by Xu and Stebbins for Li$_4$SiO$_4$.[30] In the temperature range 110–240 ^{o}C, an activation barrier of ~0.3 eV was obtained, higher than what is observed for both α-Li$_5$SiO$_4$F and γ-Li$_5$SiO$_4$F in the same temperature range. Above 240 ^{o}C, the activation barrier decreases for Li$_4$SiO$_4$ to ~0.2 eV, closer to what is observed for both α-Li$_5$SiO$_4$F and γ-Li$_5$SiO$_4$F, Fig. 11 (b) and suggesting that the Li diffusion pathways in these two phases are similar.

CONCLUSIONS

Appropriate reaction conditions to avoid loss of fluoride on heating mixtures of Li$_2$CO$_3$, LiF and SiO$_2$ have been determined. In the phase diagram Li$_2$O-LiF-SiO$_2$, the tie-line Li$_2$SiO$_3$-LiF separates those compositions that contain more SiO$_2$, and lose fluoride on heating in air at 800°C, from those that are stable under similar reaction conditions.

On the join Li_4SiO_4-LiF, a new polymorphic phase, Li_5SiO_4F, stable to ∼800 °C has been prepared and two polymorphs (α- and γ-) have been identified; XRF analysis confirmed its composition and showed that F loss did not occur during synthesis. The γ polymorph of Li_5SiO_4F was indexed on a monoclinic unit cell with parameters, a = 8.67(1), b = 16.51(1), c = 11.23(2) Å, β = 96.61(4) ° and V = 1602.3(3) Å^3.

Impedance measurements on sintered pellets showed a homogeneous bulk response with no significant grain boundary impedance. The possibility of an additional *ac* conductivity associated with dipole reorientation was detected on replotting impedance data using the permittivity formalism and an equivalent circuit containing a combination of conducting and dipolar elements was proposed and shown to fit the data well. A low frequency spike characteristic of ion blocking at the sample – electrode interface and therefore, of Li^+ ion conduction, was detected in the impedance data. From the curved nature of the spike at high temperatures and low frequencies, an estimate of the electronic transport number was made with t_e = 0.005 at 143 °C.

The α-Li_5SiO_4F polymorph shows higher Li^+ ion conductivity than the α-Li_5SiO_4F polymorph with a value of eg ∼ 1.2×10^{-7} S cm^{-1} at 40 °C. This value is several orders of magnitude higher than that of undoped Li_4SiO_4; γ-Li_5SiO_4F also has a smaller activation energy, 0.51(1) eV.

Solid state ^7Li NMR experiments indicate Li^+ mobility in both α-Li_5SiO_4F and γ-Li_5SiO_4F, highlighting its potential use as a solid electrolyte while ^{19}F NMR reveals the absence of mobile fluoride ions. Faster Li^+ ion dynamics were observed in γ-Li_5SiO_4F compared to α-Li_5SiO_4 with motional narrowing of the ^7Li NMR line shape observed at lower temperatures and smaller activation barriers for local hops over multiple timescales in relaxometry experiments. Lower activation barriers were observed for both α-Li_5SiO_4F and γ-Li_5SiO_4F compared to Li_4SiO_4 in the same temperature range, indicating improved Li^+ mobility.

The crystal structures of neither α- nor γ- polymorphs of Li_5SiO_4F are known and are under investigation; their powder XRD patterns are clearly different from that of Li_4SiO_4 and the structures cannot simply be regarded as solid solutions based on Li_4SiO_4. Both impedance measurements and ^7Li static NMR data show that the two polymorphs of Li_5SiO_4F have Li^+ diffusion properties and represent a new family of Li^+ ion conductors stable in contact with Li metal which may find possible application in thin film solid state battery development.

AUTHOR INFORMATION

Corresponding Authors:
1. b.dong@bham.ac.uk
1. a.r.west@sheffield.ac.uk
2.3. frederic.blanc@liverpool.ac.uk
Notes
The authors declare no competing financial interest.

REFERENCES

(1). Larcher, D.; Tarascon, J-M. Towards greener and more sustainable batteries for electrical energy storage. Nature Chemistry, (2014), 7, 19.

(2). Kamaya N.; Homma K.; Yamakawa Y.; Hirayama M.; Kanno R.; Yonemura M.; Kamiyama T.; Kato Y.; Hama Y.; K. Kawamoto, A. Mitsui. A lithium superionic conductor. Nature Materials, (2011), 10, 682.

(3). Hu, Y-W.; Raistrick, I.D.; Huggins, R.A. Ionic Conductivity of Lithium Orthosilicate-Lithium Phosphate Solid Solutions. Journal of the Electrochemical Society, (1977), 124, 1240.

(4). Hodge, I.M.; Ingram, M.D.; West, A.R. Ionic Conductivity of Li_4SiO_4, Li_4GeO_4, and Their Solid Solutions. Journal of the American Ceramic Society, (1976), 59, 360.

(5). Khorassani, A.; West, A.R. New Li^+ ion conductors in the system Li_4SiO_4-Li_3AsO_4. Solid State Ionics, (1982), 7, 1.

(6). Dissanayake, M.A.K.L.; West, A.R. Structure and conductivity of an Li_4SiO_4–Li_2SO_4 solid solution phase. Journal of Materials Chemistry, (1991), 1, 1023.

(7). Bates, J.B.; Dudney, N.J.; Gruzalski, G.R.; Zuhr, R.A.; Choudhury, A.; and Luck, C.F. Electrical properties of amorphous lithium electrolyte thin films. Solid State Ionics, (1992), 53-56, 647.

(8). West, A.R. Ionic conductivity of oxides based on Li_4SiO_4. Journal of Applied Electrochemistry, (1973), 3, 327.

(9). Robertson, A.D.; West, A.R.; Ritchie, A.G. Review of crystalline lithium-ion conductors suitable for high temperature battery applications. Solid State Ionics. (1997), 104, 1.

(10). Quintana, P.; Velasco, F.; West A.R. Lithium ion conducting solid solutions in the system Li_2O-Ga_2O_3-SiO_2. Solid State Ionics. (1989), 34, 149.

(11). Shannon, R.D.; Prewitt, C.T. Effective ionic radii in oxides and fluorides. Acta Crystallographica Section B, (1969), 25, 925.

(12). Recham, N.; Chotard, J-N.; Dupont, L.; Delacourt, C.; Walker, W.; Armand, M.; Tarascon J-M. A 3.6 V lithium-based fluorosulphate insertion positive electrode for lithium-ion batteries. Nature Materials, (2009), 9, 68.

(13). Khasanova, N.R.; Drozhzhin, O.A.; Storozhilova, D.A.; Delmas, C.; Antipov, E.V. New Form of Li_2FePO_4F as Cathode Material for Li-Ion Batteries Chemistry of Materials, (2012), 24, 4271.

(14). Chen, R.Y.; Ren, S.H.; Knapp, M.; Wang, D.; Witter, R.; Fichtner, M.; Hahn, H. Disordered Lithium-Rich Oxyfluoride as a Stable Host for Enhanced Li^+ Intercalation Storage. Advanced Energy Materials, (2015), 5, 1401814.

(15). Han, Y.L.; Yang, M.H.; Zhang, Y.; Xie, J.J.; Yin, D.G.; Li G.L. Tetragonal Tungsten Bronze Framework as Potential Anode for Na-Ion Batteries. Chemistry of Materials, (2016), 28, 3139.

(16). Stebbins, J.F.; Xu, Z.; D. Vollath. Cation exchange rates and mobility in aluminum-doped lithium orthosilicate: High-resolution lithium-6 NMR results. Solid State Ionics, (1995), 78, L1.

(17). Beckmann, P.A.; Dybowski, C. A Thermometer for Nonspinning Solid-State NMR Spectroscopy. Journal of Magnetic Resonance, (2000), 146, 379.

(18). Becker, Temperature dependence of NMR chemical shifts in cuprous halides. Journal of Chemical Physics, (1978), 68, 3785.

(19). Wu, J.; Kim, N.; Stebbins, J.F. Temperature calibration for high-temperature MAS NMR to 913 K: 63Cu MAS NMR of CuBr and CuI, and 23Na MAS NMR of $NaNbO_3$. Solid State Nuclear Magnetic Resonance, (2011), 40, 45.

(20). Corcoran, O., Nicholson, J.K., Wilson, I.D. Rapid multi-component detection of fluorinated drug metabolites in whole urine from a 'cassette' dose study using high resolution ^{19}F NMR spectroscopy. Analytical Communications (1999), 7, 259.

(21). Shigenobu H.; Kikuko H. Accurate Determination of NMR Chemical Shifts in Alkali Halides and Their Correlation with Structural Factors. Bulletin of the Chemical Society of Japan (1990), 63, 913.

(22). Maso, N.; West, A.R. Electronic Conductivity in Yttria-Stabilized Zirconia under a Small dc Bias. Chemistry of Materials, (2015), 27, 155

(23). Hernandez, M.A.; West, A.R. Dipolar relaxation and impedance of an yttria-stabilised zirconia ceramic electrolyte. Journal of Materials Chemistry A, (2016), 4, 1298.

(24). ZView® For Windows. Available at: http://www.scribner.com/software/68-general-electrochemistr376-zview-for-windows/

(25). Wilkening M.; Heitjans P. Extremely slow cation exchange processes in Li_4SiO_4 probed directly by two-time ^7Li stimulated-echo nuclear magnetic resonance spectroscopy. Journal of Physics: Condensed Matter (2006), 18, 9849.

(26). Böhmera R.; Jeffrey K.R.; Vogel M. Solid-state Li NMR with applications to the translational dynamics in ion conductors. Progress in Nuclear Magnetic Resonance Spectroscopy (2007), 50, 87.

(27). Heitjans, P.; Kärger, J. Diffusion in Condensed Matter, Springer-Verlag: Berlin, (2005).

(28). Kuhn, A.; Sreeraj, P.; Pöttgen, R.; Wiemhöfer, H-P.; Wilkening, M.; Heitjans, P. Li Ion Diffusion in the Anode Material $Li_{12}Si_7$: Ultrafast Quasi-1D Diffusion and Two Distinct Fast 3D Jump Processes Separately Revealed by ^7Li NMR Relaxometry. Journal of the American Chemical Society, (2011), 133, 11018.

(29). Vinod, C.C.; Heitjans, P. Chapter One - Solid-State NMR Studies of Lithium Ion Dynamics Across Materials Classes. Annual Reports on NMR Spectroscopy, (2016), 89, 1.

(30). Xu, Z.; Stebbins, J.F. Cation Dynamics and Diffusion in Lithium Orthosilicate: Two-Dimensional Lithium-6 NMR. Science, (1995), 270, 1332.

(31). Engauge Digitizer software. Available at: http://plotdigitizer.sourceforge.net

Caption of figures and tables

Fig 1 Compositions studied in the ternary system Li_2O-SiO_2-LiF; see Table S1 for results. Products obtained from compositions within the dashed triangle do not belong to this ternary system because LiF and SiO_2 are not compatible at 800 ℃.

Fig 2 Comparison of the XRD patterns, Cu Kα$_1$ radiation, of Li_4SiO_4, LiF, α−Li_5SiO_4F and γ−Li_5SiO_4F.

Fig 3. DSC results of γ−Li_5SiO_4F. The sample was heated (blue line) from 400 ℃ to 850 ℃ at 10 ℃/min under 50/50 Ar/Air atmosphere, and then cooled (green line) from 850 ℃ to 400 ℃ at 10 ℃/min under the same atmosphere.

Fig 4. Impedance data for γ−Li_5SiO_4F pellets sintered at 775 ℃ and measured in air. (a−d) complex plane plots Z*, (e) spectroscopic plots of −Z'' and M'', (f) spectroscopic plots of C'.

Fig 5. Master equivalent electrical circuit used to model the impedance data.

Fig 6. (a) Impedance complex plane plot, (b) Spectroscopic plots of C' at 95 ℃ showing fits to experimental data.

Fig 7. Impedance complex plane plot at 143 ℃ showing fit to experimental data.

Fig 8. Arrhenius plots of conductivities of Li_4SiO_4, α−Li_5SiO_4F and γ−Li_5SiO_4F. Activation energies are in eV.

Fig 9. Cyclic voltammetry test over the voltage range 0−6 V with 0.1 mV/s ramp rate.

Fig 10. ^7Li static NMR spectra of (a) α−Li_5SiO_4F and (b) γ−Li_5SiO_4F as a function of temperature.

Fig 11. (a) Temperature dependence of the ^7Li static NMR line width (full width at half maximum) of α−Li_5SiO_4F (blue) and γ−Li_5SiO_4F (red) fitted with a sigmoidal regression curve (solid line). Dashed lines indicate the onset of motional narrowing of the NMR line width. (b) Arrhenius plot of spin−lattice relaxation rates in the laboratory frame (T_1^{-1}, circle) and rotating frame ($T_{1\rho}^{-1}$, triangles) against temperature of α−Li_5SiO_4F (blue), γ−Li_5SiO_4F (red) and Li_4SiO_4 (black). Li_4SiO_4 data are obtained from Xu and Stebbins[30] and extracted using Plot Digitizer.[31] Lines are guides to the eye. Error bars are within the size of the symbols. Data below −100 ℃ are shown in Fig. S3.

Fig 12. ^{19}F static NMR spectra of (a) α−Li_5SiO_4F and (b) γ−Li_5SiO_4F as a function of temperature.

Table 1. X-ray fluorescence results of γ-Li$_5$SiO$_4$F synthesised at 775 ^{o}C.
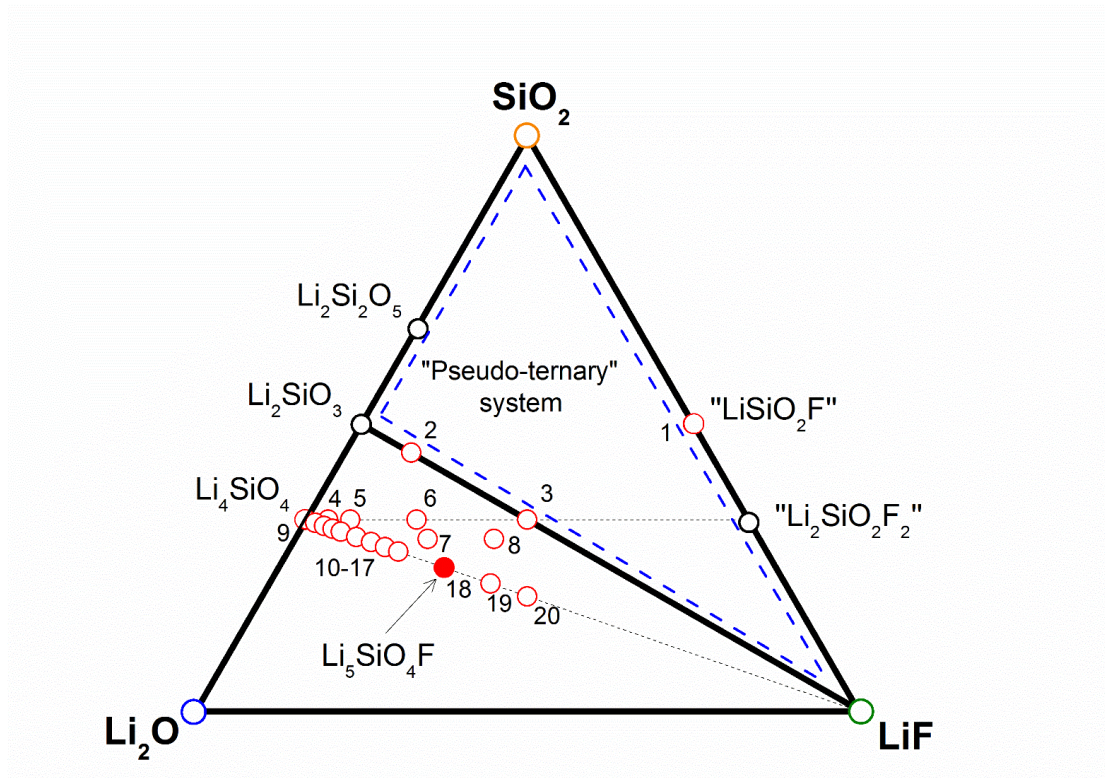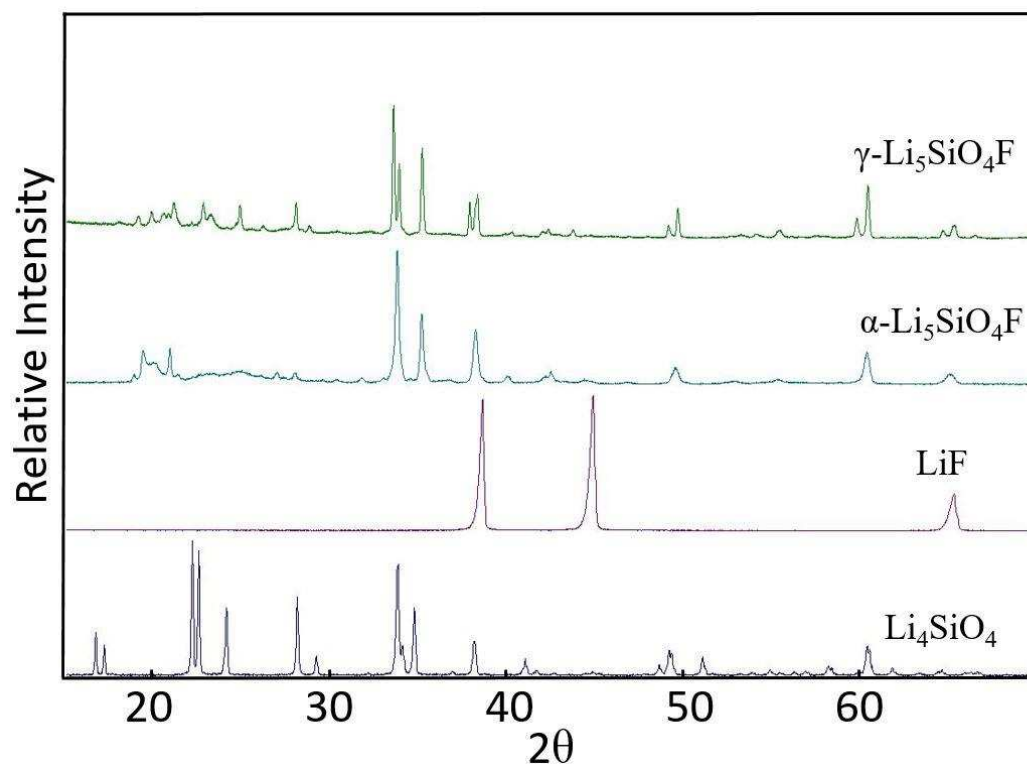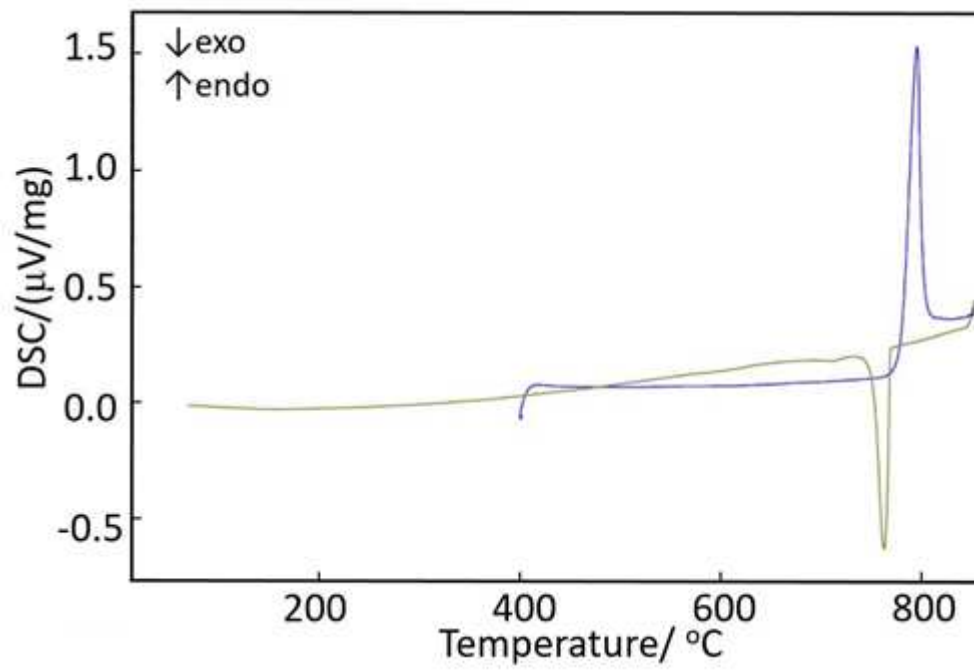
Figure 1

Figure 2

Figure 3
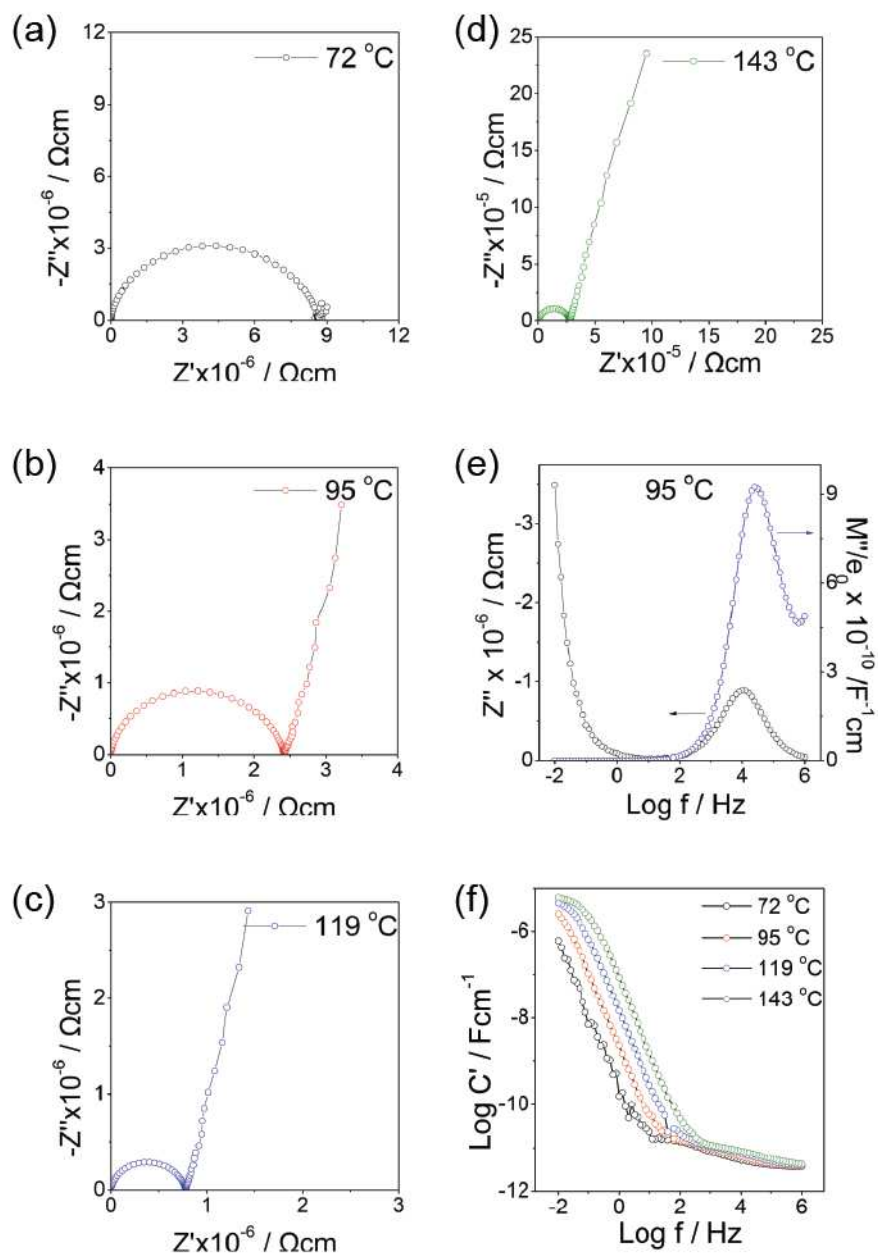
Figure 4
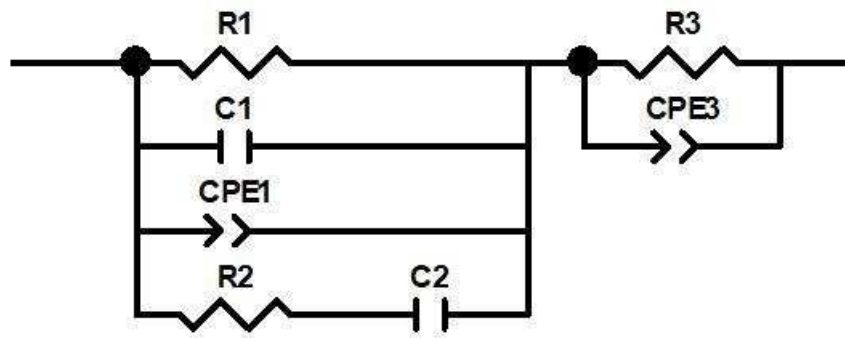
Figure 5
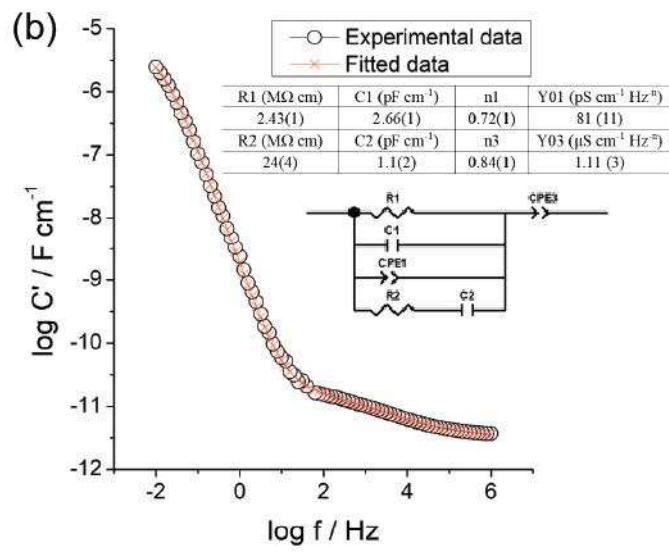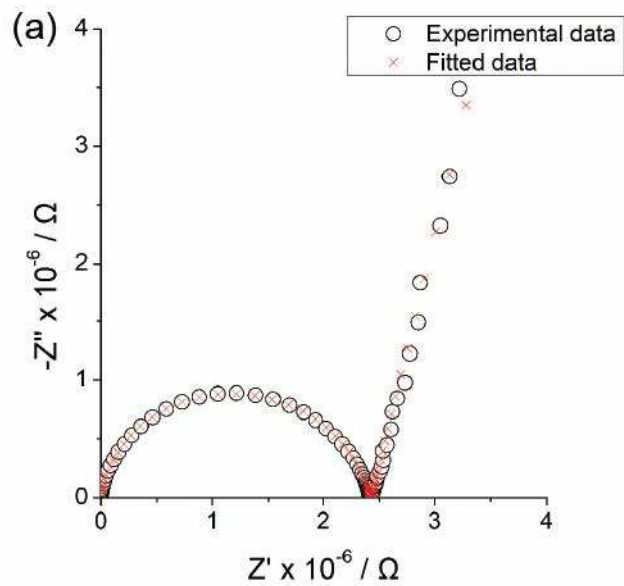
Figure 6
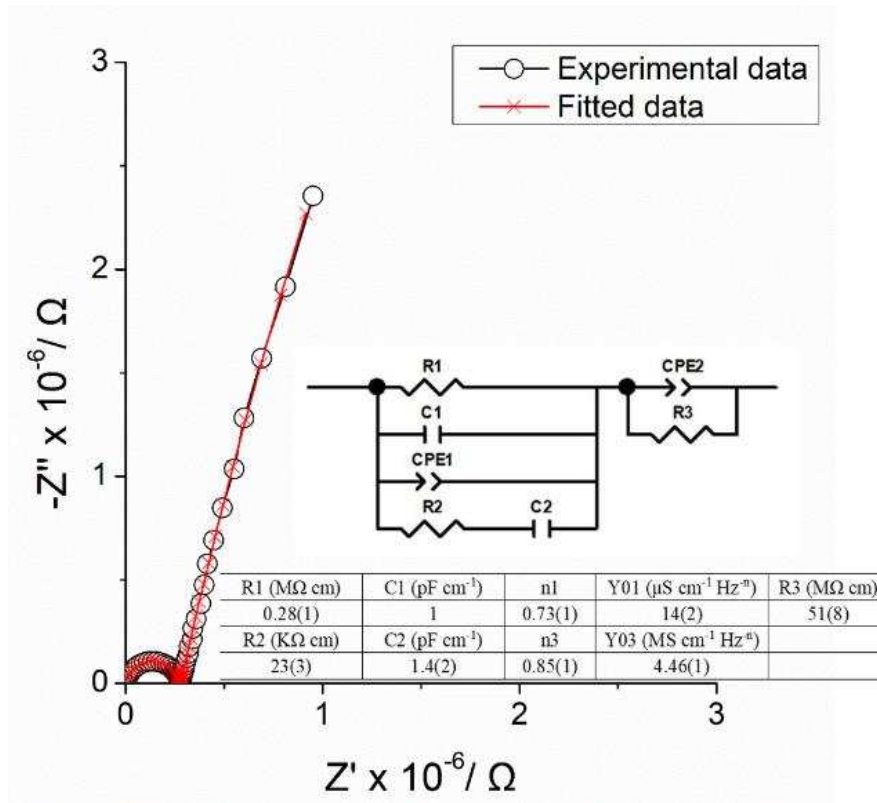
Figure 7

Figure 8

Figure 9

(a) α-Li$_5$SiO$_4$F

374 °C
301 °C
242 °C
162 °C
82 °C
21 °C
-31 °C
-92 °C

| 1000 | 500 | 0 | - 500 | -1000 |

^{7}Li /ppm

(b) γ-Li$_5$SiO$_4$F

386 °C
309 °C
232 °C
155 °C
78 °C
21 °C
-33 °C
-95 °C
-157 °C

| 1000 | 500 | 0 | - 500 | -1000 |

^{7}Li /ppm

Figure 10

Figure 11

(a) α-Li$_5$SiO$_4$F

150 °C

100 °C

50 °C

21 °C

0   - 100   - 200   - 300   - 400
^{19}F /ppm

(b) γ-Li$_5$SiO$_4$F

150 °C

100 °C

50 °C

21 °C

0   - 100   - 200   - 300   - 400
^{19}F /ppm
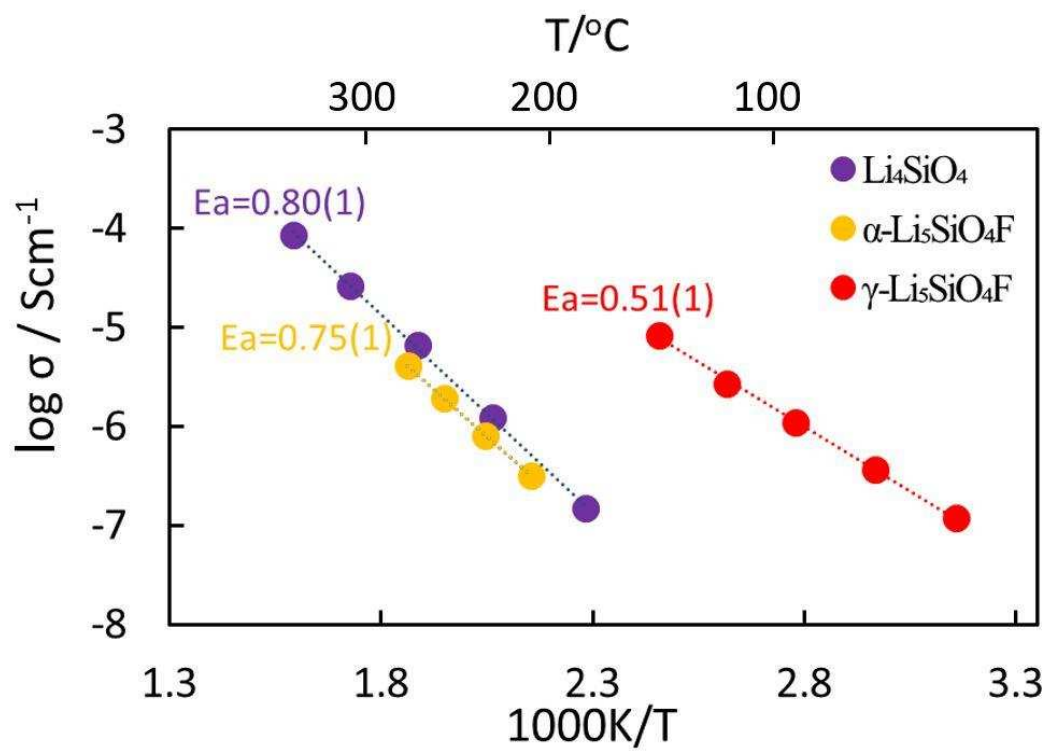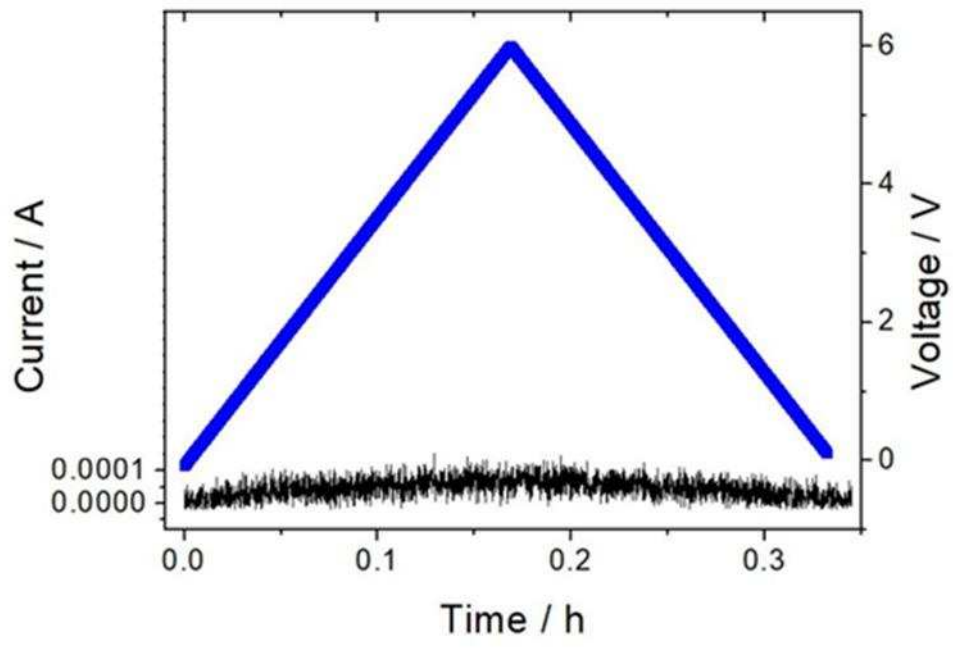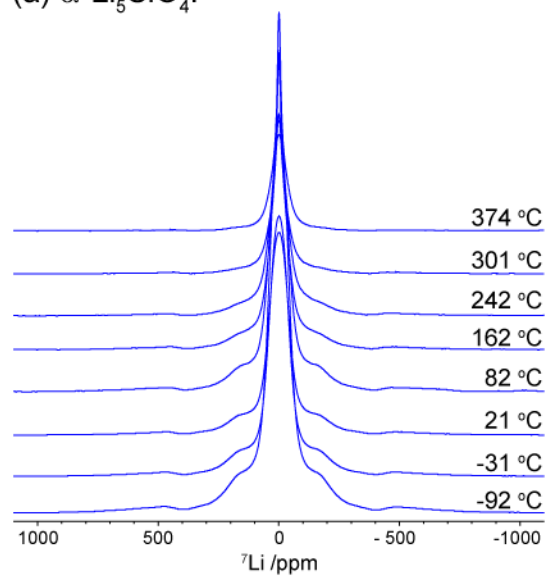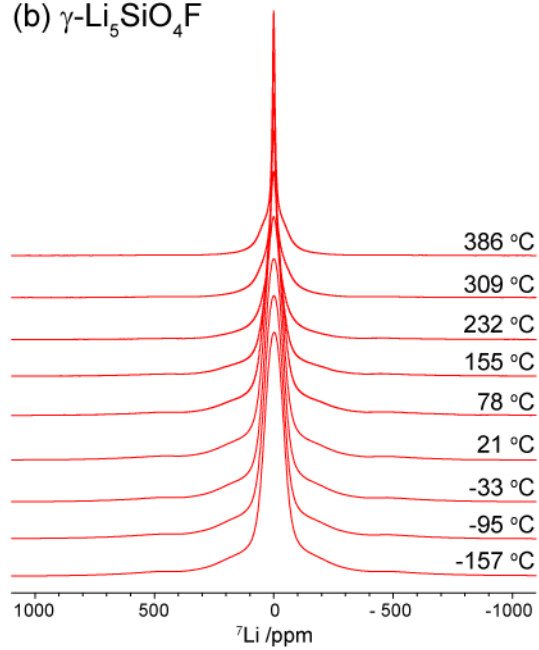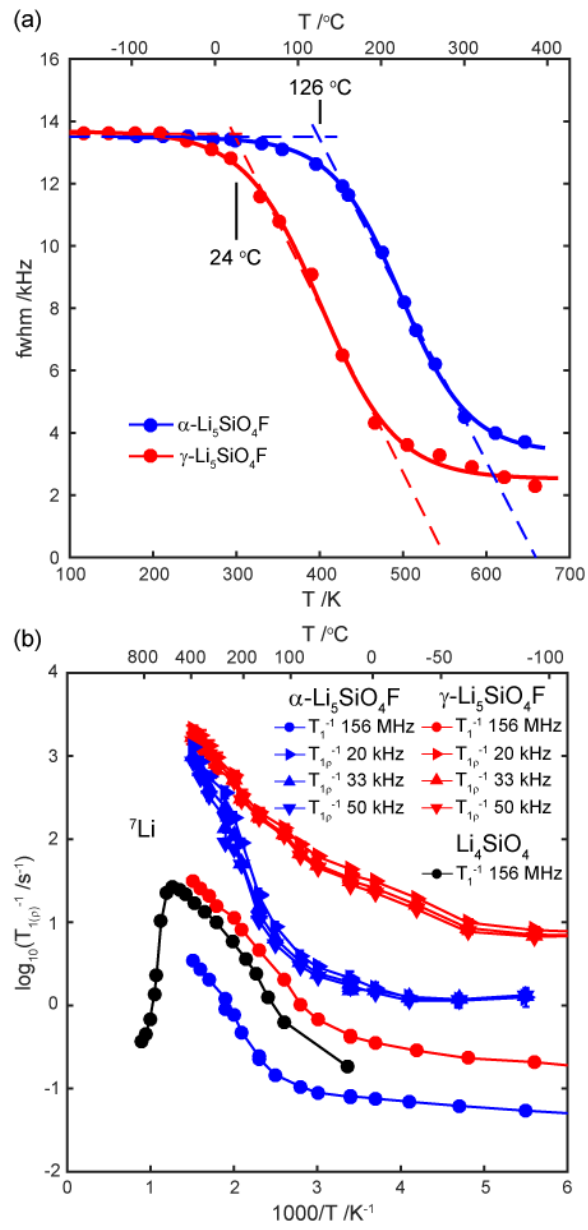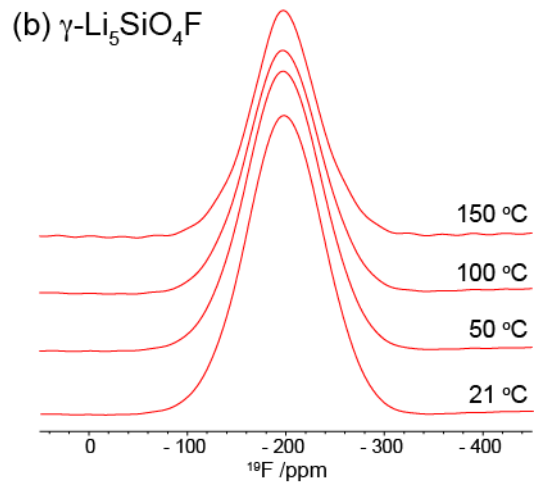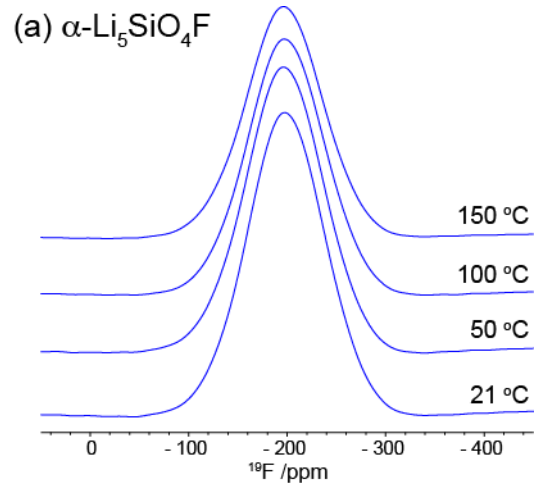
Figure 12

Table 1

Element	Experimental Concentration, weight%	Expected composition of Li_5SiO_4F, weight%
Si	18.8(8)%	19%
F	11(2)%	13%
O	45(6)%	44%